Materials Characterization 214 (2024) 114077

Contents lists available at ScienceDirect

Materials Characterization

journal homepage: www.elsevier.com/locate/matchar

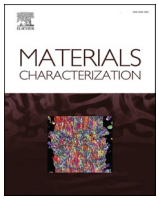

# Effects of hatch spacing on densification, microstructural and mechanical properties of β-solidifying γ-TiAl alloy fabricated by laser powder bed fusion

Sung-Hyun Park [a], Ozkan Gokcekaya [a,b], Myung-Hoon Oh [c], Takayoshi Nakano [a,b,*]

[a] Division of Materials and Manufacturing Science, Graduate School of Engineering, Osaka University, 2-1, Yamadaoka, Suita, Osaka 565-0871, Japan
[b] Anisotropic Design & Additive Manufacturing Research Center, Osaka University, 2-1, Yamadaoka, Suita, Osaka 565-0871, Japan
[c] School of Materials Science and Engineering, Kumoh National Institute of Technology (KIT), 61 Daehakro, Gumi, Gyeongbuk 39177, Republic of Korea

ARTICLE INFO

*Keywords:*
γ-TiAl alloy
Hatch spacing
Microstructure evolution
Densification
Laser powder bed fusion
Mechanical properties

ABSTRACT

β-solidifying γ-titanium aluminide (γ-TiAl) alloys, which typically contain β-phase stabilizers such as Nb and Cr, hold great promise for the aerospace industry and can potentially be processed through additive manufacturing to realize performance unachievable using conventional methods. However, the effects of laser powder bed fusion (L-PBF) parameters on the characteristics of the thus obtained samples remain underexplored. To address this gap, we herein examined the effects of hatch spacing on the densification, microstructural, and mechanical properties of L-PBF-fabricated Ti-44Al-6Nb-1.2Cr (at.%) alloy samples, revealing that the strong influence on thermal history induced the variation in densification and formation of two microstructure types. 0.01 mm hatch spacing resulted in repetitive slow cooling and sufficiently remelting, thus suppressing crack formation, promoting high densification, and inducing a complex phase transformation involving the formation of a basket-weave-structured $\alpha_2$ phase and the ⟨001⟩ alignment of the β phase along the build direction. 0.06 mm hatch spacing resulted in rapid cooling and insufficient heat accumulation, favoring the massive phase transformation, a jagged morphology $\alpha_2$ phase with a randomly distributed crystallographic texture. Hardness was mainly correlated with phase constitution and volume fraction, whereas compressive properties were jointly determined by additional effects of multiple factors such as grain size and crystallographic texture. This work provides the fundamental insights required to suppress defect formation in β-solidifying γ-TiAl alloys and tailor their microstructure for mechanical property enhancement.

## 1. Introduction

Given their high creep resistance, low density, and superior high-temperature performance, γ-titanium aluminide (γ-TiAl) alloys are a promising alternative to the superalloys currently used in the aerospace industry [1,2], as exemplified by the use of the conventional Ti-48Al-2Nb-2Cr (48–2-2 alloy, at.%) alloy to produce low-pressure turbine blades for engines [3]. However, the low maximum service temperature (~750 °C) of this alloy results in a narrow application range, thus requiring improvement through alloy design and processing optimization [2,3].

The recently developed β-solidifying γ-TiAl alloys contain large amounts of β-stabilizers such as Nb, Cr, and Mo, which shift the α-transus line to the Al-rich side and thus favor complete solidification via the β phase affording a homogeneous microstructure with a low segregation degree [4,5]. At high temperatures, these alloys form a disordered β phase with a body-centered cubic lattice providing a sufficient number of slip systems and thus enabling the application of conventional forming techniques such as hot-die forging [6,7]. Moreover, the selection of optimal forming conditions and subsequent heat treatment results in high- and low-temperature mechanical properties superior to those of the 48–2-2 alloy [3,8]. However, such techniques exhibit the drawbacks of additional precise cutting and surface treatment, limited design freedom, and large amounts of generated waste. These problems can be mitigated through the processing of γ-TiAl alloys and/or other metallic materials using additive manufacturing, which affords

* Corresponding author at: Division of Materials and Manufacturing Science Graduate School of Engineering, Osaka University, 2-1 Yamadaoka, Suita, Osaka 565-0871, Japan.
*E-mail address:* nakano@mat.eng.osaka-u.ac.jp (T. Nakano).

https://doi.org/10.1016/j.matchar.2024.114077
Received 8 November 2023; Received in revised form 10 June 2024; Accepted 11 June 2024
Available online 13 June 2024

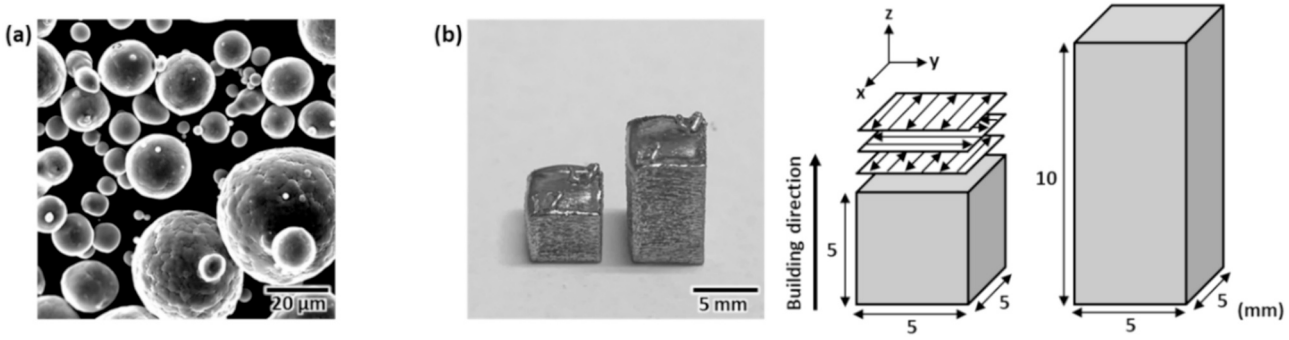


**Fig. 1.** (a) Typical SEM image of the Ti-44Al-6Nb-1.2Cr alloy powder and (b) specimen appearance and fabrication schematic.

specimens outperforming those produced using conventional techniques [9–11].

Metal-based additive manufacturing processes can be categorized according to the material feeding system and energy source [12], with the detailed characteristics of each category described elsewhere [13]. Depending on the energy source, powder bed systems can be classified as electron beam powder bed fusion (EB-PBF) and laser powder bed fusion (L-PBF). Given that γ-TiAl alloys are highly cracking-susceptible and intrinsically brittle intermetallics, they are usually processed by EB-PBF and not L-PBF, as the former method involves preheating to a high temperature and can therefore effectively relieve the thermal stress due to rapid cooling and suppress crack formation [14,15]. While L-PBF machines equipped with high-temperature-preheating systems are not yet well established and require increased capital investments. However, the smaller beam and powder size in L-PBF than EB-PBF process can increase the processing accuracy and surface quality of the product, respectively [16]. More importantly, different manufacturing conditions such as the temperatures of thermal cycles and preheating conditions result in different microstructure characteristics and variations of the mechanical properties. In the case of 48–2-2 alloy, a homogenous and fine microstructure can be obtained by the L-PBF process, and the mechanical properties were enhanced compared to the EB-PBF process [17]. Thus, the adoption of L-PBF process in γ-TiAl alloy could provide opportunities for the expansion of the γ-TiAl alloy applications, which still requires the realization of industrial-level densification of components [18].

From the aforementioned, γ-TiAl alloys are easy to crack during the L-PBF process because of the excessive thermal stress that cannot accommodate [19,20]. The substrate preheating, remelting, and scan strategy/length adjustment can be considered in the L-PBF process to eliminate cracking resulting from thermal stress [18,21–23]. In addition, the laser power, scanning speed, layer thickness, and hatch spacing can be adjusted to optimize the input of energy density. Hatch spacing, i.e., the distance between two adjacent scan tracks in the same layer, determines the overlap between these tracks more directly than other L-PBF parameters. In L-PBF-processed Al alloys, the regions of sufficient overlap between adjacent scan tracks act as stress-release regions and show the lowest residual stress [24]. Hatch spacing influences the evolution of pore defects from keyholes (improperly closed pores) to unfused ones, thus affecting densification [25]. Moreover, hatch spacing affects the phase transformation pathway and/or phase composition and is therefore closely related to mechanical performance [25,26].

Recently, several researchers reported that the L-PBF process can be applied to fabricate γ-TiAl alloys [20,27], their results demonstrated the process parameters were closely related to the crack inhibition behaviors. Especially, the variation of hatch spacings in a single layer related to microstructural evolution and mechanical properties proposed the importance of microstructure tailoring by approaching hatch spacing control to enhance performance in β-solidifying γ-TiAl alloy [28]. among the various process parameters, given hatch spacings, which help to accumulate heat and prevent/refill defects, can be an important process parameter to γ-TiAl alloy that has not yet been comprehensively investigated. Therefore, we first chose Ti-44Al-6Nb-1.2Cr (at.%) alloy, which can expect homogeneous microstructure and improved mechanical properties as the β-solidifying γ-TiAl alloy [29], and focused on the effects of hatch spacings on the relative density of samples fabricated by the L-PBF to achieve high densification and minimize crack formation. Furthermore, the effect of hatch spacing on thermal history was examined to understand the distribution of residual strain and microstructural characteristics such as phase volume fraction and morphology. The correlation between microstructure and mechanical properties was discussed.

## 2. Materials and methods

### 2.1. Specimen fabrication

The gas-atomized Ti-44Al-6Nb-1.2Cr alloy powder (Osaka Titanium Technologies, Japan) contained spherical particles with a mean diameter of 36.0 μm (Fig. 1a). The composition of this alloy was determined as balance Ti, 43.77 at.% Al, 5.96 at.% Nb, and 1.22 at.% Cr by inductively coupled plasma optical emission spectroscopy. Fig. 1b shows the appearance and schematic depiction of the specimens fabricated by L-PBF (EOS M290, EOS, Germany) for microstructural (5 mm × 5 mm × 5 mm) and mechanical property (5 mm × 5 mm × 10 mm) characterizations. Depending on the process parameters, a bulged surface can be found on the top of the specimens due to high laser energy input, indicating that difficult to ensure structural integrity for complex geometries, and/or results in deterioration of printability. Therefore, it is suggested that additional research would be required to establish dimensional accuracy and reduction of the surface roughness which might cause fabrication failure to extend this study. The detailed L-PBF fabrication condition was under argon (<100 ppm $O_2$) using a laser power of 180 W, layer thickness of 0.06 mm, scanning speeds of 600–1000 mm/s, and hatch spacings of 0.01–0.06 mm. The baseplate was kept at 200 °C, and bidirectional scanning with a rotation of 90° between layers was used to minimize residual stress [30].

### 2.2. Microstructure observation

The specimens were sectioned in the *y*-*z* plane, and the cross sections were polished with SiC paper and an alumina suspension. Microstructural features, including internal defects such as pores and cracks, were observed using optical microscopy (OM; BX60, Olympus, Japan), field-emission scanning electron microscopy (SEM; JIB-4610F, JEOL, Japan) coupled with energy-dispersive X-ray spectroscopy (EDS; X-Max$^N$, Oxford Instruments, UK) and electron backscatter diffraction (EBSD; NordlysMax$^3$, Oxford Instruments, UK) analysis (NordlysMax$^3$, Oxford Instruments, UK), and transmission electron microscopy (TEM; JEM-3010, JEOL, Japan). Relative densities and phase volume fractions

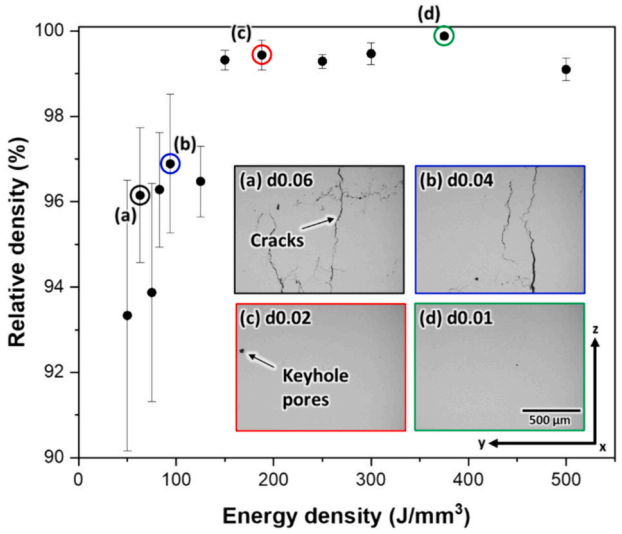


**Fig. 2.** Relative density–volumetric energy density plot with insets (a)–(d) showing representative OM images of *y*-*z*-cross sectioned specimens fabricated using different hatch spacings (d0.01–d0.06).

were determined from OM and SEM images using ImageJ software.

### 2.3. Numerical simulations of thermal history

The temperature variation of multi-scan tracks was estimated for different hatch spacings using a finite element thermal model simulation (COMSOL Multiphysics 6.1, COMSOL Inc., Sweden) following the detailed methodology introduced in previous studies, and the simulated molten pool shape and experimental single track were compared to ensure reliability [28,31]. A Gaussian distribution ($Q$) of the laser beam was adopted:

$$Q = \frac{4AP}{\pi R^2 H} exp\left(-\frac{2r^2}{R^2}\right)\left[1-\frac{z}{H}\right] \ (0 < z < H) \quad (1)$$

where $P$ is the laser power, $R$ is the laser beam radius, $r$ is the distance between the center of the laser beam and the powder bed surface, $A$ is the laser absorption rate, $H$ is the laser penetration depth, and $z$ is the depth. At least 15 multitracks were performed in a single layer. The predicted temperature distribution was measured at the top surface of the same number of $n^{th}$ multitracks under all conditions to compare the equivalent time progress.

### 2.4. Mechanical property testing

Vickers hardness (HMV-G, Shimadzu, Japan) and nanoindentation (ENT-1100a, ELONIX, Japan) tests were performed in the *x*-*y* plane. The specimen surfaces were coarse-polished with SiC paper and mirror-polished with an alumina suspension to exclude the influence of surface roughness. The former test was carried out using a test force of 0.2 kgf and a holding time of 15 s, while the latter test was performed using a Berkovich tip at a force of 4.9 mN and a holding time of 10 s. Room-temperature compressive tests (AG-X, Shimadzu, Japan) were conducted in air at a nominal strain rate of $1.7 \times 10^{-4}$ $s^{-1}$. Specimens with dimensions of 2 mm × 2 mm × 5 mm were cut from the center of 5 mm × 5 mm × 10 mm cuboids using electrical discharge wire cutting. The compressive load was applied parallel to the 5-mm-edge (i.e., build) direction. The results were expressed as means ± standard deviations.

## 3. Results and discussion

### 3.1. Densification and crack prevention

Fig. 2 shows the relative density of the fabricated samples as a function of the applied volumetric energy density (VED), which can be expressed as

$$\text{VED} = \frac{P}{v \bullet d \bullet t} \quad (2)$$

Here, $P$ is the laser power, $v$ is the scanning speed, $d$ is the hatch spacing, and $t$ is the layer thickness. An appropriate VED is required to achieve high densification during L-PBF. Insufficient energy input (low VED) results in the lack of fusion defects due to the existence of unmelted powders and/or insufficient remelting of the previous scan layer [32], whereas excessive energy input (high VED) leads to low densification because of gas entrapment and/or keyhole formation [33]. Similarly, the increasing tendency of the relative density can be observed with increasing the VED and optimized at 375 J/mm$^3$. However, further excessive VED induces a decrease of the densification.

To reveal the effects of VED on sample properties, we prioritized hatch spacing over other process parameters to achieve heat accumulation and prevent crack formation. Samples fabricated using hatch spacings of 0.01, 0.02, 0,04, and 0.06 mm were denoted as d0.01, d0.02, d0.04, and d0.06, respectively. The OM images of *y*-*z*-cross sectioned specimens (Fig. 2a–d) revealed that with variation hatch spacing, the number of cracks and spherical pores decreased, while the relative

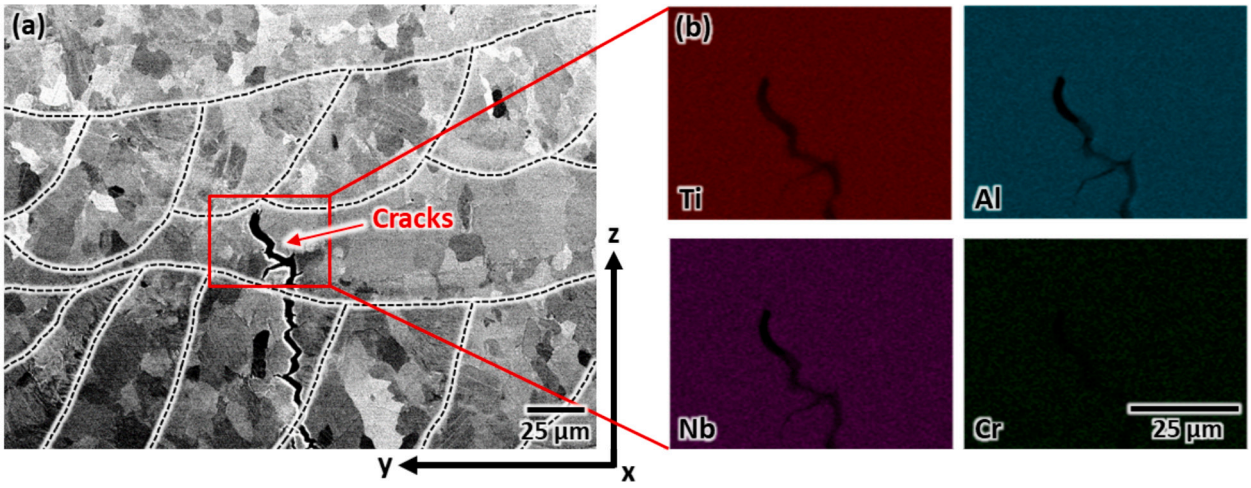


**Fig. 3.** (a) SEM-BSE image of d0.06 showing the crack initiation region and (b) the corresponding distributions of alloy elements. The dashed lines mean melt pool boundaries.

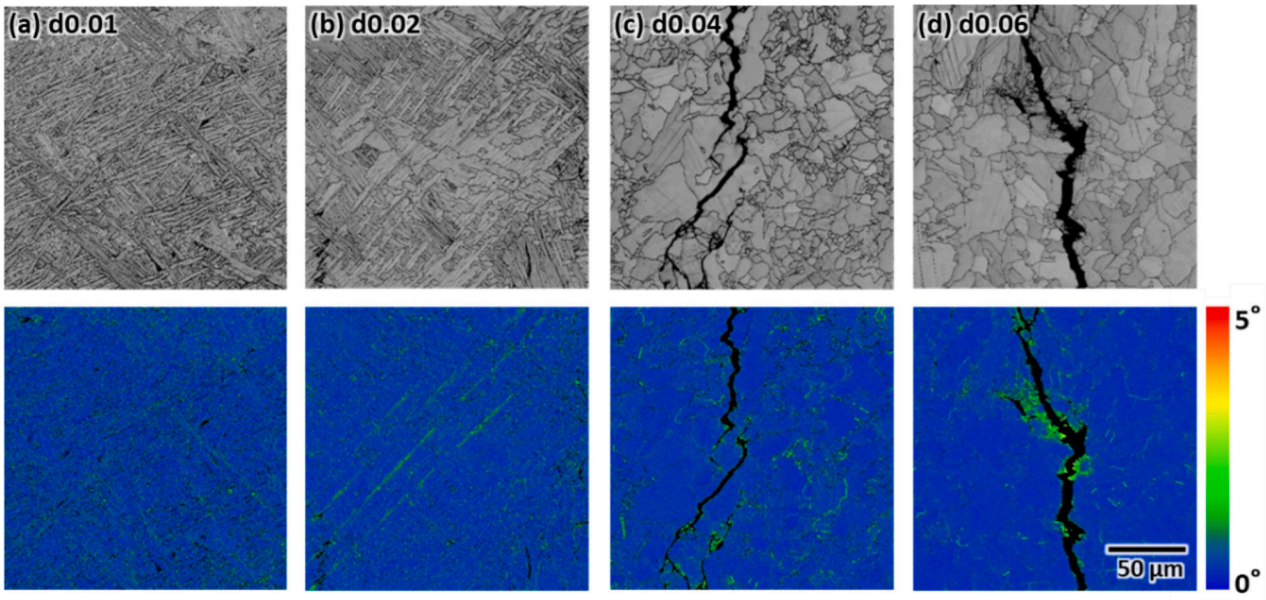


**Fig. 4.** Results of SEM-EBSD analysis including band contrast and KAM maps for (a) d0.01, (b) d0.02, (c) d0.04, and (d) d0.06.

density increased from 96.15 ± 1.58% (d0.06, Fig. 2a) to 99.88 ± 0.07% (d0.01, Fig. 2d). As mentioned previously, the typical defects observed under suboptimal L-PBF conditions include unfused regions, pores, and cracks [32]. The lack of fusion and porosity are relatively easy to mitigate by process parameter optimization, whereas the elimination of cracks, which is indispensable for satisfying industrial requirements, is challenging [34,35]. Crack-free γ-TiAl products fabricated by L-PBF have been rarely reported, and the determination of a process window affording highly dense γ-TiAl specimens is difficult [20,36].

To identify the reason for crack prevention at d0.01 and d0.02, we observed cracks in d0.06. The SEM-back-scattered electron (BSE) imaging of this specimen revealed crack propagation along grain boundaries and a variation in the contrast of the matrix $\alpha_2$ phase due to differences in grain orientations (Fig. 3a). The rapid cooling during L-PBF does not provide sufficient time for the segregation of alloy elements but allows for microsegregation, which increases susceptibility to cracking [34]. Inhomogeneous Al content variations resulting from evaporation and segregation may promote cracking at the phase interface because they affect the final distribution of the β, $\alpha_2$, and γ phases [37], which have different thermal expansion coefficients [38]. However, the EDS analysis revealed the absence of element segregation in the crack region (Fig. 3b), demonstrating that it might not be the main factor responsible for crack formation. Moreover, β-solidifying γ-TiAl alloys resulted in Al and Nb distributions considerably more homogeneous than those achieved using other solidification modes (e.g., the peritectic reaction or single-α-phase region in the as-cast state) [5].

The crack initiation point was located in the band-shaped *y*-direction scan track (Fig. 3a). Cracks perpendicular to the scan direction (transverse cracks), mainly caused by the large thermal stress below the ductile-to-brittle transition temperature, were previously observed in a γ-TiAl alloy under single-track conditions [19]. These results imply that crack formation can be ascribed to large thermal and residual stresses. Fig. 4(a–d) shows the band contrast and kernel average misorientation (KAM) maps obtained for different hatch spacings. At the microscale, KAM mapping is an efficient technique for estimating residual strain, which appears as local variations in the lattice orientation [18,39]. This KAM was obtained by calculating the average misorientation between the measured and neighboring spots. The area corresponding to high-misorientation spots (yellowish-green) gradually increased with increasing hatch spacing; in particular, the residual strain spots were

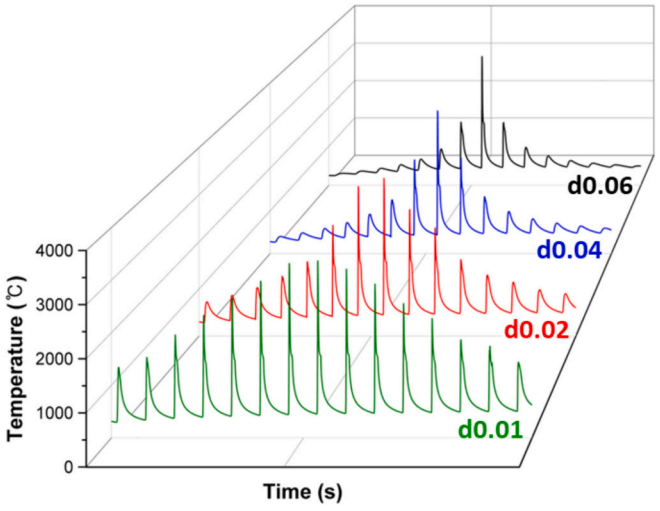


**Fig. 5.** Numerical simulated temperature–time plots of multi-scan tracks for d0.01–d0.06.

clearly visible in the crack-surrounding regions. Thus, the main cause of crack formation was identified as high residual stress.

The high densification without crack initiation and low residual stress observed for d0.01 and d0.02 can be rationalized as following two aspects. At first, although the high preheating temperature (~800 °C) of EB-PBF effectively relieves thermal and residual stresses [14,15], current L-PBF systems are incapable of reaching such high preheating temperatures. However, the adoption of an appropriate hatch spacing can reduce residual stress owing to the sufficient overlap regions increasing the overall temperature and number of defect remelting regions [24]. Thus, hatch spacing optimization can be used to adjust heat accumulation. At d0.01 and d0.02, the increase in heat accumulation due to the close proximity of neighboring scan tracks leads to slower cooling, a similar effect is expected for preheating; thus, the residual stress substantially decreases at lower cooling rates [22,40]. To validate this hypothesis, we investigated the temperature history using numerical simulations. Fig. 5 depicts the temperature history of multi-scan tracks for different hatch spacings, revealing that the maximum

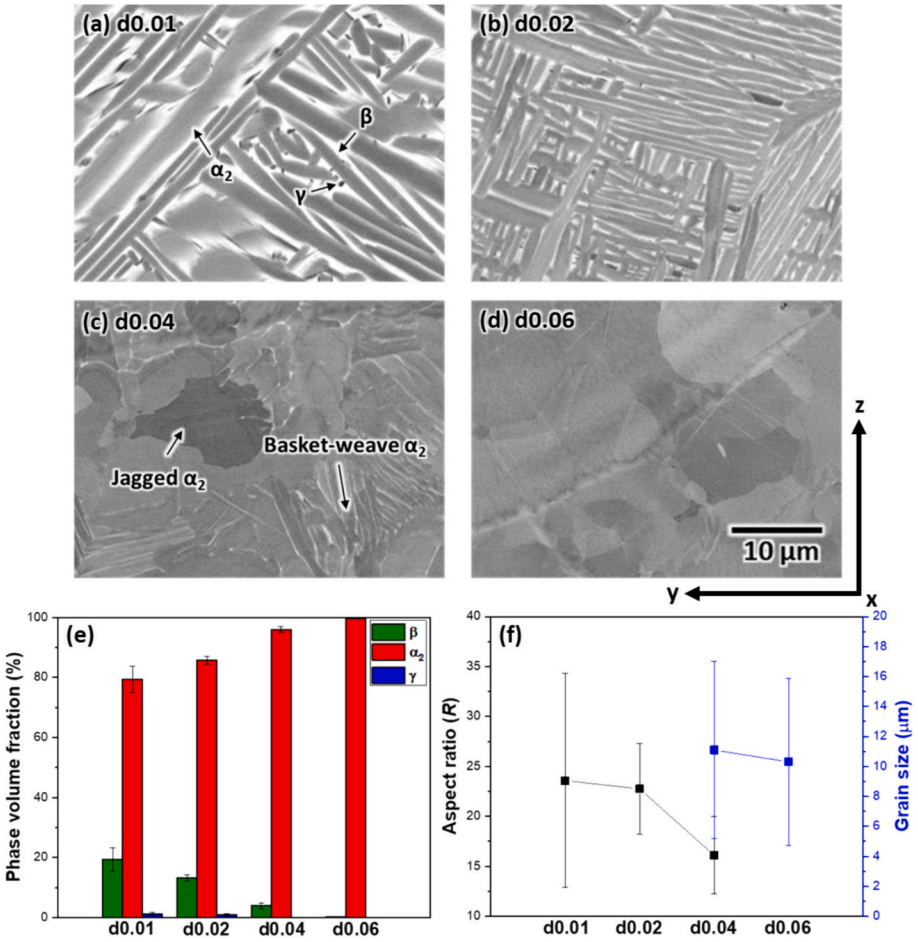


**Fig. 6.** (a–d) SEM-BSE images, (e) phase volume fractions, (f) mean aspect ratios and grain size of $\alpha_2$ phase for d0.01–d0.06.

temperature peaks of the scan tracks, which are the standard measurement tracks of the temperature distribution, are almost identical under all conditions, whereas the temperature distributions of the adjacent scan tracks are different. At d0.01, the cooling rate until without the heat accumulation by adjacent scan tracks was $1.12 \times 10^4$ K/s, a relatively slower temperature decrease was observed owing to the accumulation of heat caused by the adjacent scan track; thus, lower residual stress is expected as mentioned above. On the other hand, when the hatch spacing is increased to d0.06, the cooling rate got higher to $6.05 \times 10^4$ K/s. Therefore, the effect of heat accumulation from adjacent scan tracks will decrease and experience a faster temperature decrease inducing higher residual stress, which corresponds to KAM measurements (Fig. 4).

Secondly, the excessive overlap between two adjacent scan tracks results in deeper melt pools, causing the formation of keyhole pores because of gas entrapment and/or metal vapor [33,41]. However, the existing pores and initiate cracks can simultaneously be refilled by partially remelted melt pools [42], which explains the high relative densities of d0.01 and d0.02.

### 3.2. Microstructure characterization

Fig. 6(a–d) shows the four types of distinct microstructures observed in *y-z* cross-sectioned samples fabricated under conditions identical to those used to prepare the specimens in Section 3.1, revealing that the transitions of these microstructures depend on the hatch spacing. Therefore, the dependence of thermal history on hatch spacing was closely correlated with sample microstructure.

The SEM-BSE images of d0.01–d0.06 indicated the presence of β (white), $\alpha_2$ (gray), and γ (black) phases. Moreover, d0.01 mainly contained the basket-weave-structured $\alpha_2$ phase and small γ-phase regions (<1 μm) distributed in the β phase. In d0.02, the basket-weave morphology was preserved, but the thickness of the $\alpha_2$-phase regions and the volume fraction of the β phase decreased. Upon a further hatch spacing increase to 0.04 mm, the $\alpha_2$-phase regions became considerably thinner, and the β phase almost disappeared. In addition, the newly developed morphology of the $\alpha_2$ phase coexisted with jagged grain boundaries, which is typical of massive transformation [43]. In d0.06, the β phase almost entirely disappeared, and only the massively transformed $\alpha_2$ phase was observed. Fig. 6e shows the volume fractions of the three phases observed in d0.01–d0.06. As the hatch spacing increased from 0.01 to 0.06 mm, the volume fraction of the β phase decreased from 19.4% to 0.2%, while those of the $\alpha_2$ and γ phases increased from 79.4% to 99.8% and decreased from 1.2% to 0%, respectively. Fig. 6f presents the effects of hatch spacing on the aspect ratio (*R*, length of major axis/length of minor axis) and grain size of the $\alpha_2$ phase, revealing that the *R* decreased from 23.6 ± 10.7 to 16.1 ± 3.8 when the hatch spacing increased from d0.01 to d0.04. For the basket-weave-structured $\alpha_2$ phase, the average length of the minor axis did not substantially change, whereas the length of the major axis noticeably decreased, as it was limited by the primary β-grain size [44]. Thus, the formation of larger primary β grains owing to high energy input accounted for the high aspect ratio of the $\alpha_2$ phase. Low energy input induced the change of $\alpha_2$ phase micromorphology from basket-weave to jagged. The ratio of the basket-weave-structured to massively transformed $\alpha_2$ phase was approximately 3:7 in d0.04, and the grain size of the massively transformed $\alpha_2$ phase decreased from 11.1 ± 5.9 to 10.3 ± 5.6 μm when the energy input further decreased with an increase in hatch spacing from

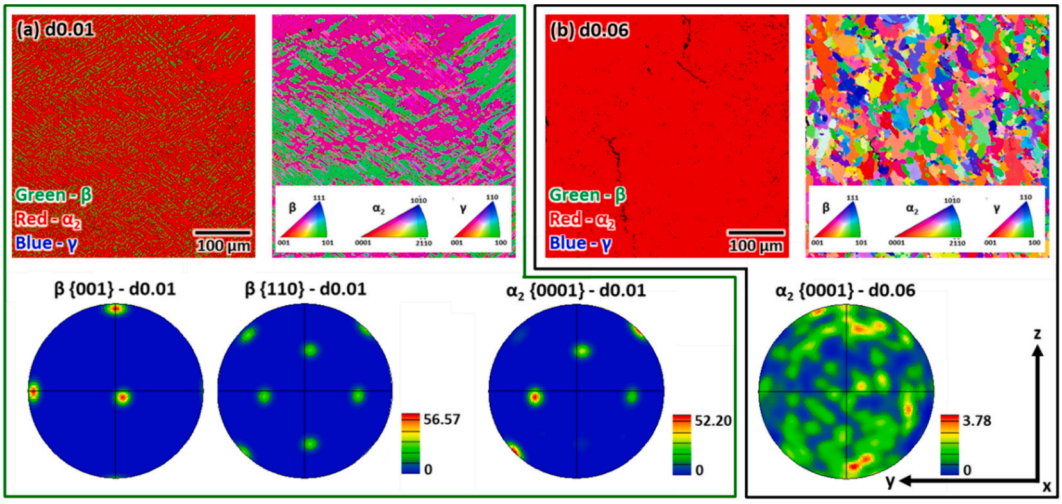


**Fig. 7.** Phase maps, inverse pole figure maps, and pole figures for (a) d0.01 and (b) d0.06.

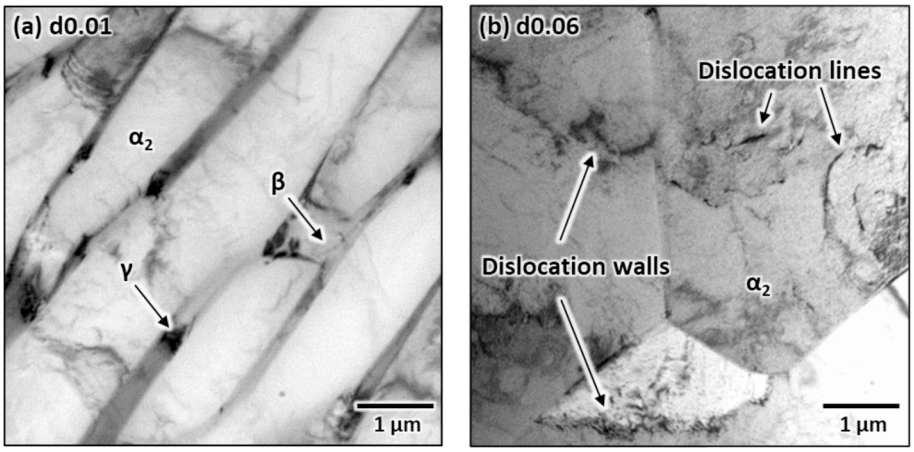


**Fig. 8.** Bright-field TEM images of (a) d0.01 and (b) d0.06 revealing the higher densification of dislocation components in (b).

d0.04 to d0.06.

Fig. 7a and b show the results of SEM-EBSD analysis, including phase maps, inverse pole figure maps, and pole figures, for d0.01 and d0.06. Minor phases such as the γ phase in d0.01 and the β and γ phases in d0.06 are not represented because of their small amounts. According to the pole figures, the crystallographic texture of β-phase in d0.01 exhibits strong <001> alignment along the build direction, which is a frequently observed feature of L-PBF [10,45,46]. Furthermore, the overlaid $\{110\}_\beta$ and $\{0001\}_{\alpha 2}$ directions in the pole figures imply compliance with the Burgers orientation relationship (Burgers OR) expressed as follows [47]:

$$\{110\}_\beta \,//\, (0001)_\alpha \text{ and } \langle 111\rangle_\beta \,//\, <11\bar{2}0>_\alpha \tag{3}$$

Therefore, the observed basket-weave-structured $\alpha_2$ phase is inclined by approximately ± 45° relative to the build direction because of the <001> alignment of the β phase and their crystallographic relationship. By contrast, the crystallographic texture of the $\alpha_2$ phase in d0.06 is randomly distributed because of the massive transformation. The parent and child phases formed by massive transformations do not maintain an orientation relationship [48], which implies the cooling rate is an important contribution to the formation of crystallographic texture in β-solidifying γ-TiAl alloy. Similarly, the massive transformation can be observed under a high cooling rate manufacturing process such as the gas-atomization process [49], the parent and child phases were not crystallographically aligned [50].

The microstructural differences between d0.01 and d0.06 were further observed by TEM. The predominant $\alpha_2$ lath and the small size of the γ-phase regions in the β-phase matrix were observed in d0.01, whereas the $\alpha_2$ phase was mainly visible in d0.06 (Fig. 8), which corresponded to the results of SEM-BSE analysis (Fig. 6). Few dislocation tangles in the $\alpha_2$ lath, i.e., low stress-induced deformation were occurred for d0.01, whereas the $\alpha_2$ phase grains in d0.06 contained numerous dislocation lines and walls, as previously reported for massively transformed microstructure obtained after quenching [51]. This behavior means that the residual stress was not efficiently relieved owing to the fast cooling rate.

Fig. 9 presents the microstructural evolution mechanisms for the two typical microstructure types in the L-PBF-processed β-solidifying γ-TiAl alloy. The microstructural evolution upon the repeated heating and cooling during L-PBF was divided into five stages according to the phase transformation sequences based on the pseudo-phase diagram (Fig. 9a and b). For d0.01 (Fig. 9b), the microstructure created by the previous scan tracks entirely melted to afford the liquid phase, as the peak temperature of the first cycle exceeded the solid-liquid temperature during reheating. The β phase solidified from the liquid (below solidus temperature) upon cooling and was directly transformed into the massive α phase (Fig. 9c and d)), i.e., the β → α + β phase separation in the α + β phase region was skipped because of the fast cooling [9]. Herein, excessive residual stress due to the rapid solidification of the L-PBF process induced crack initiation along the massive α grain boundaries.

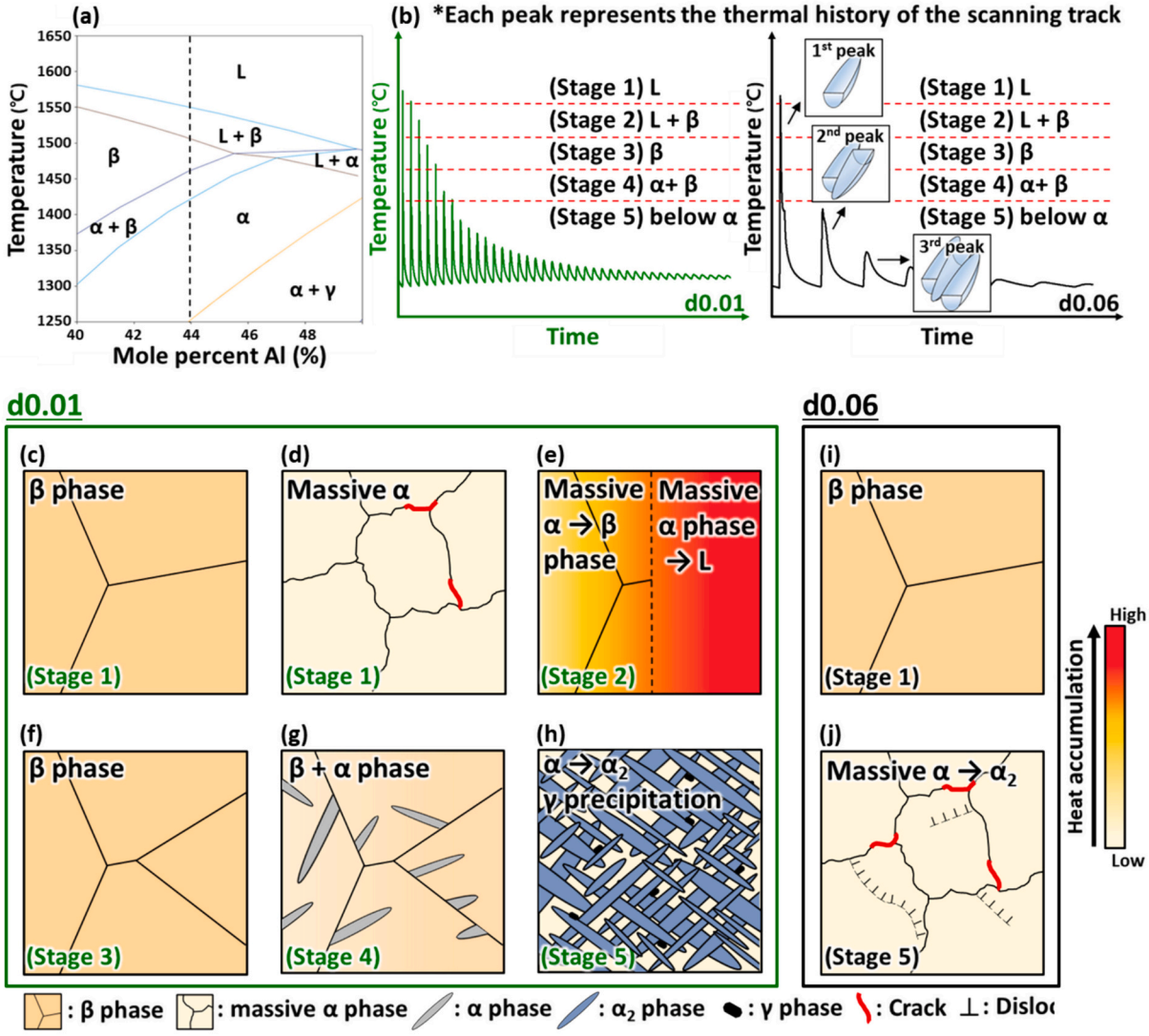


**Fig. 9.** Schematic microstructural evolution during laser powder bed fusion based on the thermal history obtained for d0.01 and d0.06.

However, a part of the massive α phase including the cracks experienced partial remelting can eliminate the defects and the new β phase is solidified (Fig. 9e and f). Furthermore, the α phase nucleated at the β phase grain boundaries according to Burgers orientation relationship when the temperature reaches the α + β region (Fig. 9g). This initially formed α phase could extend into subsequently solidified regions through epitaxial growth and coarsening until unaffected by the further subsequent layer reheating and/or remelting [44]. In addition, the continuous thermal exposure below the α phase region induced the phase transformation of α → $\alpha_2$ phase and precipitation of the minor γ phase (Fig. 9h). By contrast, d0.06 (Fig. 9b) showed a simple thermal history and experienced the L → L + β → β → massive α phase transformation as identical with d0.01, which is not following the Burgers orientation relationship between β and α phases (Fig. 9i and j). However, the peak temperature of the second cycle could not reach different phase regions, i.e., remained below the α-phase regions. Thus, the occurred defects during the solidification still exist, phase transformation can occur in the massive α → $\alpha_2$ phase and only the grain size differed according to the reheats and/or remelts, while the remaining dislocations formed dislocation walls and lines such as those shown in Fig. 8b.

**Table 1**
Summarized mechanical properties of d0.01–d0.06.

| | d0.01 | d0.02 | d0.04 | d0.06 |
|---|---|---|---|---|
| Vickers hardness (HV0.2) | 506.2 ± 4.8 | 433.8 ± 10.6 | 466.5 ± 5.6 | 483.6 ± 12.5 |
| Yield strength (MPa) | 1173.2 ± 29.52 | 1214.7 ± 19.4 | 1256.1 ± 21.6 | 1342.3 ± 4.68 |
| Compressive strength (MPa) | 1422.6 ± 20.4 | 1470.3 ± 16.8 | 1512.6 ± 2.7 | 1544.8 ± 13.8 |
| Compressive strain (%) | 13.1 ± 0.2 | 13.3 ± 0.8 | 8.7 ± 0.5 | 8.5 ± 0.7 |

### 3.3. Mechanical properties

Table 1 lists the mechanical properties of d0.01–d0.06. Initially, we determined the nanoindentation hardness of the β phase (7.8 ± 0.1 GPa) and basket-weave-structured $\alpha_2$ phase (7.2 ± 0.1 GPa) in d0.01 and that of the massively transformed $\alpha_2$ phase (7.6 ± 0.4 GPa) in d0.06 (Fig. 10a). Similar to a previous study, the β phase was much harder than the basket-weave-structured $\alpha_2$ phase [52]. However, the nano hardness of the massively transformed $\alpha_2$ phase considerably exceeded that of the basket-weave-structured $\alpha_2$ phase and was similar to that of the β phase owing to the large residual stress increasing the density of dislocations

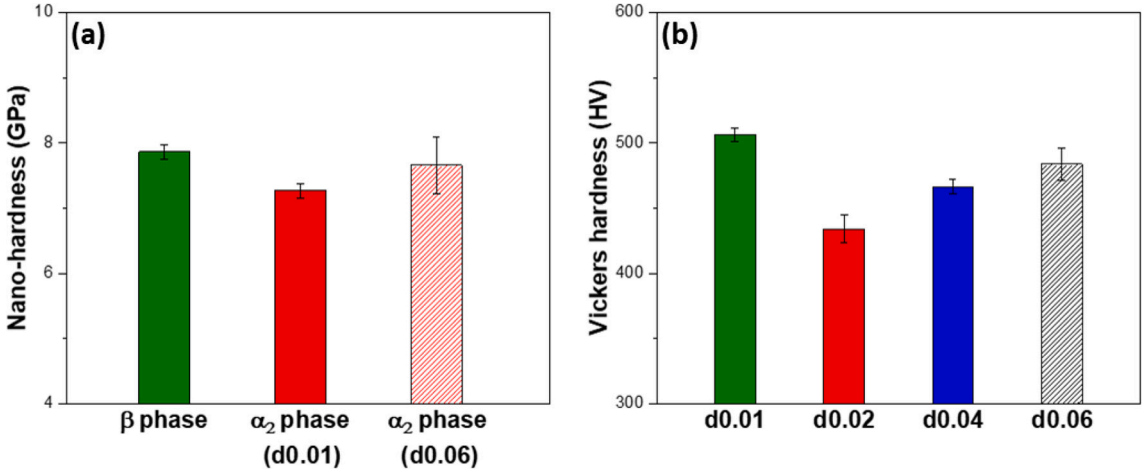


**Fig. 10.** (a) Nanoindentation hardnesses of the β phase, basket-weave-structured $\alpha_2$ phase in d0.01, and massively transformed $\alpha_2$ phase in d0.06. (b) The effect of hatch spacing on Vickers hardness.

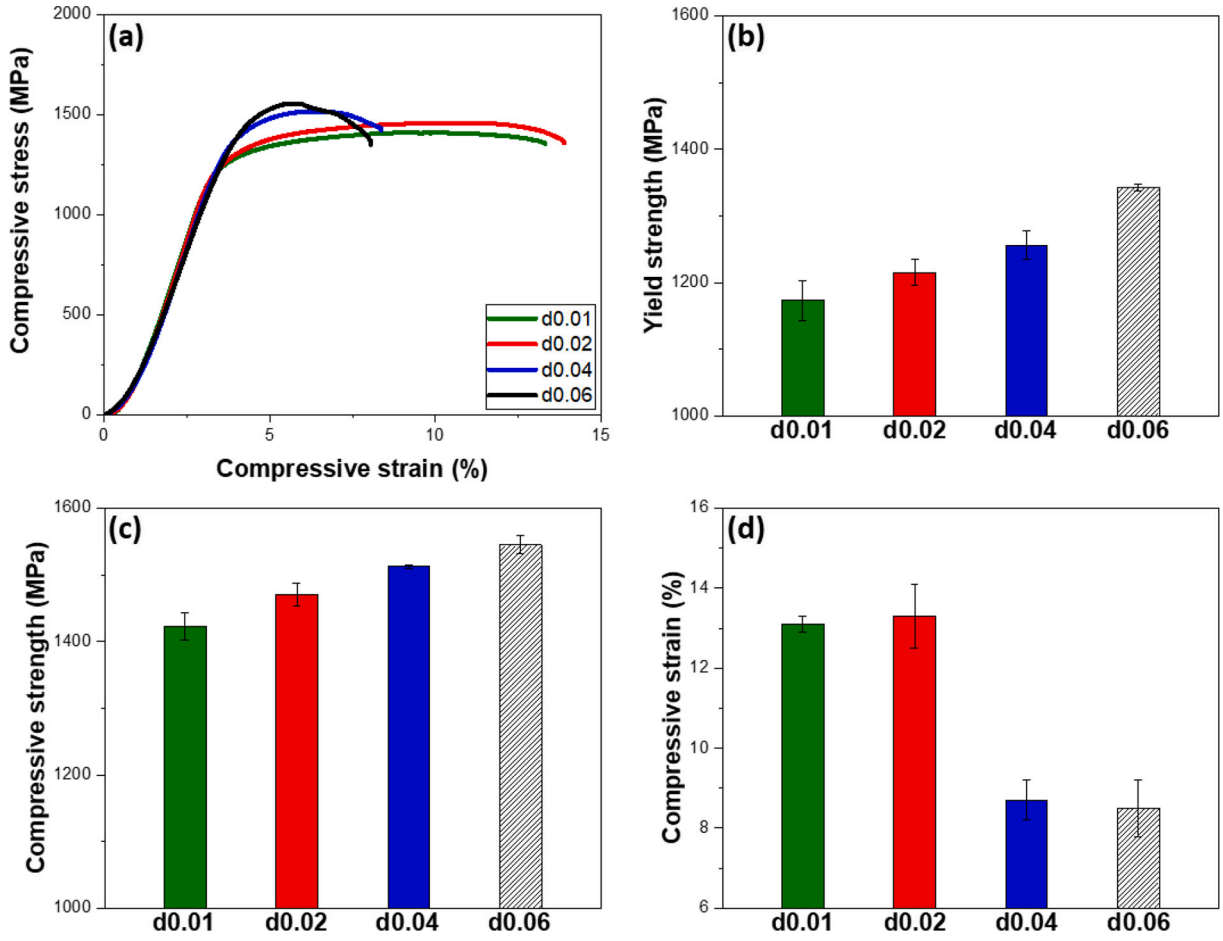


**Fig. 11.** (a) Room-temperature compressive strength–strain curves, (b) yield strengths, (b) compressive strengths, and (d) compressive strains of d0.01–d0.06.

(Fig. 8b). Since the hardness of existing phases in descending order is β > massively transformed $\alpha_2$ > basket-weave-structured $\alpha_2$ phase, the variation in Vickers hardness depending on hatch spacing can be explained by considering the nano hardness results of these phases with their distribution in the measurement area. Because Vickers hardness is primarily determined from the volume fraction of the existing hard phases such as β phase and massively transformed $\alpha_2$ phase regarding the Vickers indenter interacting with an area [27]. As can be seen, the β phase and massively transformed $\alpha_2$ phase showed higher hardness than the basket-weave-structured $\alpha_2$ phase, therefore, the larger volume fraction in β and/or massively transformed $\alpha_2$ phase will lead to the increase in the Vickers hardness. Indeed, the high Vickers hardness values were measured in d0.01 (506.2 ± 4.8 HV) and d0.06 (483.6 ± 12.5 HV), which contained a large volume fraction of hard β phase and/or massively transformed $\alpha_2$ phase, while d0.02 (433.8 ± 10.6 HV) was lowest due to less amount of hard phase (Fig. 10b).

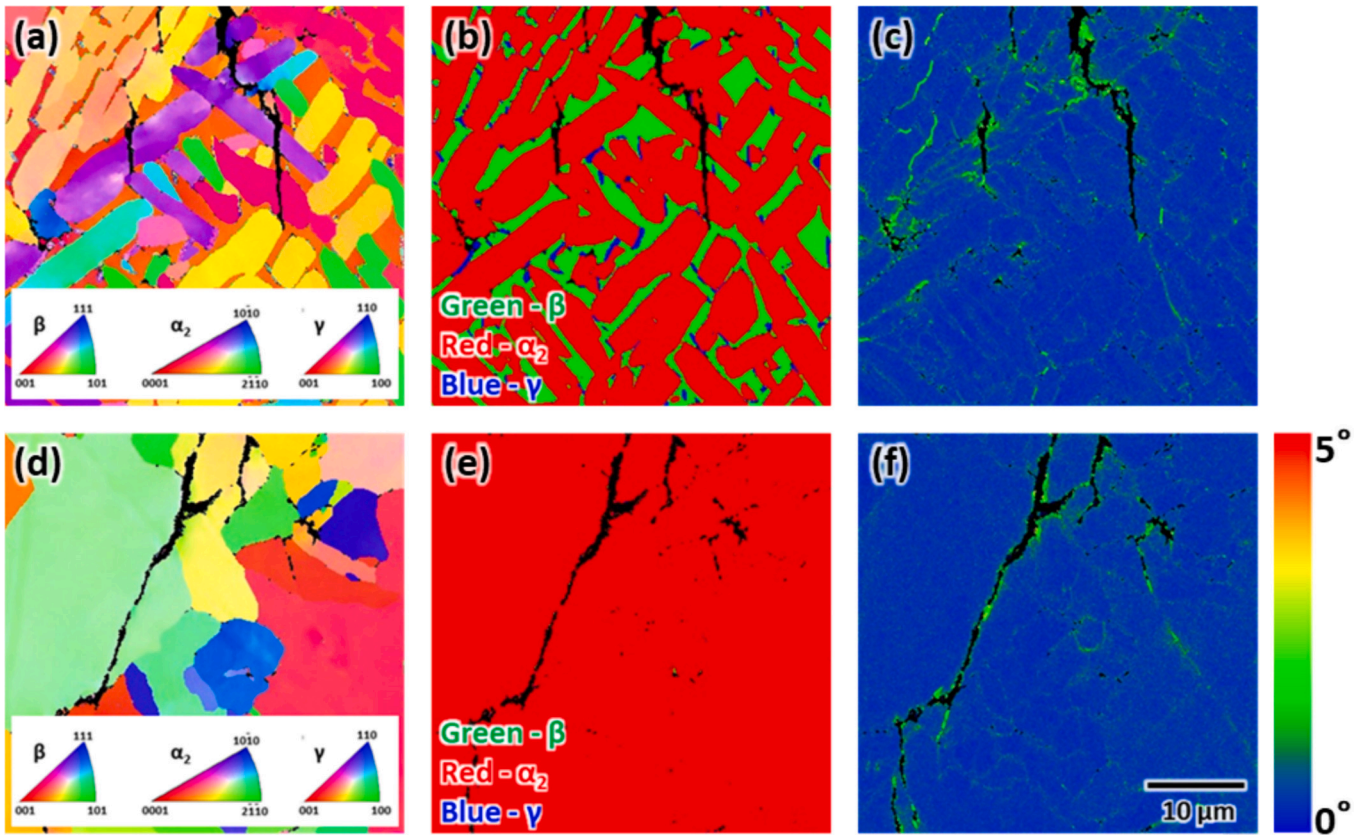


**Fig. 12.** (a,d) Inverse pole figure, (b,e) phase, and (c,f) KAM maps acquired near the microcrack regions in (a–c) d0.01 and (d–f) d0.06 after compressive testing.

Fig. 11 displays the compressive stress-strain curves and compressive yield strengths, strengths, and compressive strains of d0.01–d0.06. The yield strengths and compressive strengths gradually increased with increasing hatch spacing (Fig. 11b and c). No significant correlation was shown with the Vickers hardness because the compressive properties indicate the behavior of the material upon compression, which is different from local deformation. Therefore, although phase constitution and volume fraction are an important contribution to the strengthening mechanisms, the Hall-Petch (grain refining) principle and crystallographic texture development were additionally contribute to the strenghtening. At first, grain boundaries induce the formation of dislocation pile-ups and thus increase the stress required to propagate dislocations to the neighboring grains according to the Hall-Petch principle [53]. For d0.01, the *R* of $\alpha_2$ phase was 23.6 ± 10.7, which is the highest among all conditions, and hence, the number of $\beta/\alpha_2$-phase interfaces attributed to acting similarly to grain boundaries was lowest. While the microstructural morphology changed to the massively transformed $\alpha_2$ phase with increasing hatch spacing, the grain size was the lowest at d0.06 as 10.3 ± 5.6 μm, which more frequently impedes the movement of dislocations (Fig. 6f). On the other hand, the crystallographic texture development also exhibited differences in strength (Fig. 7). The strong texture indicated that adjacent grains shared crystallographic features, which decreased the energy demand of dislocation propagation. In addition, the main constitution $\alpha_2$ phase in d0.01, which is formed by ⟨100⟩ alignment of the β phase and followed by Burgers OR showed relatively low compressive yield strength because of the anisotropic mechanical behavior with the operation slip system on the prism and/or basal planes [54]. By contrast, the randomly distributed texture in d0.06 has a chance to frequently hinder dislocation movement and contain the oriented $\alpha_2$ phase with higher yield strength. Therefore, not only the phase constitution and volume fraction but also the additional effect of grain refining and developed crystallographic texture are attributed to the variation of yield strength and compressive strengths because of the volumetric property.

Upon compressive testing, d0.04 and d0.06 were expected to exhibit premature fracturing due to pre-existing cracks (Fig. 11d), even if compressive testing was relatively insensitive to microcracks. However, the exploration of crack propagation is essential to further advance the microstructure and increase damage tolerance. Fig. 12 shows the microcrack regions in compression-tested d0.01 and d0.06, revealing the formation of deformation-induced transgranular cracks due to intrinsic brittleness in both cases. During deformation, cracking can be initiated at the $\beta/\alpha_2$-phase interface in d0.01 because of the incompatibility of plasticity between the two phases. On the other hand, the critical resolved shear stress of the randomly distributed $\alpha_2$ phase in d0.06 strongly depends on the slip mode, i.e., the insufficient number of active slip systems limits ductility and crack initiation [54]. Note that microcrack propagation stopped at the adjacent β-phase region in d0.01, i.e., the harder β phase disturbed crack growth [55]. In d0.06, cracks continuously propagated along the grain boundaries and/or inside the grains; thus, this type of microstructure without preexisting cracks was also expected to have a lower damage tolerance.

The above results indicate the benefits of using d0.01 and d0.02 to achieve high densification and balanced mechanical properties. Furthermore, the use of larger hatch spacings can potentially enhance mechanical performance if crack formation can be suppressed. These findings help establish the competitiveness of L-PBF usage and guide microstructure tailoring in β-solidifying γ-TiAl alloys. However, how the crystallographic texture and subsequent heat treatment influence high-temperature mechanical properties is still required to be investigated. To the best of our knowledge, the crystallographic texture remains stable after heat treatment up to 1200 °C [56], even when the grain size increases. In addition, subsequent heat treatment forms an $\alpha_2/\gamma$ lamellar microstructure. The features of this microstructure such as $\alpha_2/\gamma$ lamellar orientation or spacing strongly influence mechanical behavior [57,58]. Thus, future studies should examine the effect of the crystallographic

texture of the β-solidifying γ-TiAl alloy processed by L-PBF and subsequent heat treatment on high-temperature mechanical properties, and the results will be reported in due course.

## 4. Conclusions

The effects of L-PBF parameters, especially hatch spacing, on the densification, microstructure, and mechanical properties of a β-solidifying γ-TiAl alloy were examined. Depending on the hatch spacing, high densification can be achieved over 99.5% of relative density, furthermore, microstructural evolution mechanisms and mechanical properties were addressed, focusing particularly on microstructural characteristics. The following main conclusions can be drawn:

1. Densification was strongly affected by process parameters and maximized at d0.01, which can be explained as follows. (i) The intense increase in temperature due to the thermal influence from adjacent scan tracks decelerated cooling and effectively released the residual stress. (ii) The partially remelted pools refilled defects such as existing pores and cracks.
2. Different microstructures originated in the as-built state, depending on the hatch spacing. The repetitive heating and cooling at the d0.01 induced complex phase transformations and the formation of a predominantly basket-weave microstructure with a strongly developed crystallographic texture, whereas the d0.06 induced a simple phase transformation and rapid cooling, resulting in a massively transformed microstructure with a randomly distributed crystallographic texture.
3. Hardness was determined by the phase constitution and volume fraction. The hardness of the high-dislocation-density massively transformed $\alpha_2$ phase was similar to that of the β phase, which is the hardest phase in the examined alloy. The results of compressive testing highlighted the additional effects of multiple factors such as phase grain size, and crystallographic texture. As a result, balanced mechanical properties and better damage tolerance were achieved by the use of d0.01 and d0.02.

## CRediT authorship contribution statement

**Sung-Hyun Park:** Investigation, Data curation, Formal analysis, Writing – original draft. **Ozkan Gokcekaya:** Conceptualization, Methodology, Validation, Supervision, Writing – review & editing. **Myung-Hoon Oh:** Conceptualization, Writing – review & editing. **Takayoshi Nakano:** Conceptualization, Resources, Supervision, Funding acquisition.

## Declaration of competing interest

The authors declare that they have no known competing financial interests or personal relationships that could have appeared to influence the work reported in this paper.

## Data availability

The raw/processed data required to reproduce these findings can be shared upon request.

## Acknowledgment

This work was supported by a Grants-in-Aid for Scientific Research (grant number JP23H00235) from the Japan Society for the Promotion of Science (JSPS) and CREST-Nanomechanics: Elucidation of macroscale mechanical properties based on understanding nanoscale dynamics of innovative mechanical materials (Grant Number: JPMJCR2194) from the Japan Science and Technology Agency (JST).

## References

[1] F. Appel, U. Brossmann, U. Christoph, S. Eggert, P. Janschek, U. Lorenz, J. Müllauer, M. Oehring, J.D.H. Paul, Recent progress in the development of gamma titanium aluminide alloys, Adv. Eng. Mater. 2 (2000) 699–720.
[2] Y.-W. Kim, S.-L. Kim, Advances in gammalloy materials–processes–application technology: successes, dilemmas, and future, JOM 70 (2018) 553–560, https://doi.org/10.1007/s11837-018-2747-x.
[3] B.P. Bewlay, S. Nag, A. Suzuki, M.J. Weimer, TiAl alloys in commercial aircraft engines, Mater. High Temp. 33 (2016) 549–559, https://doi.org/10.1080/09603409.2016.1183068.
[4] H. Clemens, S. Mayer, Design, processing, microstructure, properties, and applications of advanced intermetallic TiAl alloys, Adv. Eng. Mater. 15 (2013) 191–215, https://doi.org/10.1002/adem.201200231.
[5] X. Ding, L. Zhang, J. He, F. Zhang, X. Feng, H. Nan, J. Lin, Y.W. Kim, As-cast microstructure characteristics dependent on solidification mode in TiAl-Nb alloys, J. Alloys Compd. 809 (2019), https://doi.org/10.1016/j.jallcom.2019.151862.
[6] H. Clemens, W. Wallgram, S. Kremmer, V. Güther, A. Otto, A. Bartels, Design of novel β-solidifying TiAl alloys with adjustable β/B2-phase fraction and excellent hot-workability, Adv. Eng. Mater. 10 (2008) 707–713, https://doi.org/10.1002/adem.200800164.
[7] W. Wallgram, T. Schmölzer, L. Cha, G. Das, V. Güther, H. Clemens, Technology and mechanical properties of advanced γ-TiAl based alloys, Int. J. Mater. Res. 100 (2009) 1021–1030, https://doi.org/10.3139/146.110154.
[8] S. Bolz, M. Oehring, J. Lindemann, F. Pyczak, J. Paul, A. Stark, T. Lippmann, S. Schrüfer, D. Roth-Fagaraseanu, A. Schreyer, S. Weiß, Microstructure and mechanical properties of a forged β-solidifying γ TiAl alloy in different heat treatment conditions, Intermetallics 58 (2015) 71–83, https://doi.org/10.1016/j.intermet.2014.11.008.
[9] K. Cho, H. Kawabata, T. Hayashi, H.Y. Yasuda, H. Nakashima, M. Takeyama, T. Nakano, Peculiar microstructural evolution and tensile properties of β-containing γ-TiAl alloys fabricated by electron beam melting, Addit. Manuf. 46 (2021) 102091, https://doi.org/10.1016/j.addma.2021.102091.
[10] O. Gokcekaya, N. Hayashi, T. Ishimoto, K. Ueda, T. Narushima, T. Nakano, Crystallographic orientation control of pure chromium via laser powder bed fusion and improved high temperature oxidation resistance, Addit. Manuf. 36 (2020) 101624, https://doi.org/10.1016/j.addma.2020.101624.
[11] O. Gokcekaya, T. Ishimoto, S. Hibino, J. Yasutomi, T. Narushima, T. Nakano, Unique crystallographic texture formation in Inconel 718 by laser powder bed fusion and its effect on mechanical anisotropy, Acta Mater. 212 (2021) 116876, https://doi.org/10.1016/j.actamat.2021.116876.
[12] J. Akram, P. Chalavadi, D. Pal, B. Stucker, Understanding grain evolution in additive manufacturing through modeling, Addit. Manuf. 21 (2018) 255–268, https://doi.org/10.1016/j.addma.2018.03.021.
[13] W.E. Frazier, Metal additive manufacturing: a review, J. Mater. Eng. Perform. 23 (2014) 1917–1928, https://doi.org/10.1007/s11665-014-0958-z.
[14] W. Kan, B. Chen, C. Jin, H. Peng, J. Lin, Microstructure and mechanical properties of a high Nb-TiAl alloy fabricated by electron beam melting, Mater. Des. 160 (2018) 611–623, https://doi.org/10.1016/j.matdes.2018.09.044.
[15] M. Todai, T. Nakano, T. Liu, H.Y. Yasuda, K. Hagihara, K. Cho, M. Ueda, M. Takeyama, Effect of building direction on the microstructure and tensile properties of Ti-48Al-2Cr-2Nb alloy additively manufactured by electron beam melting, Addit. Manuf. 13 (2017) 61–70, https://doi.org/10.1016/j.addma.2016.11.001.
[16] S.H. Sun, K. Hagihara, T. Ishimoto, R. Suganuma, Y.F. Xue, T. Nakano, Comparison of microstructure, crystallographic texture, and mechanical properties in Ti–15Mo–5Zr–3Al alloys fabricated via electron and laser beam powder bed fusion technologies, Addit. Manuf. 47 (2021), https://doi.org/10.1016/j.addma.2021.102329.
[17] K. Mizuta, Y. Hijikata, T. Fujii, K. Gokan, K. Kakehi, Characterization of Ti-48Al-2Cr-2Nb built by selective laser melting, Scr. Mater. 203 (2021), https://doi.org/10.1016/j.scriptamat.2021.114107.
[18] O. Gokcekaya, T. Ishimoto, T. Todo, R. Suganuma, R. Fukushima, T. Narushima, T. Nakano, Effect of scan length on densification and crystallographic texture formation of pure chromium fabricated by laser powder bed fusion, Crystals 11 (2021) 1–14, https://doi.org/10.3390/cryst11010009.
[19] S. Lee, J. Kim, J. Choe, S.W. Kim, J.K. Hong, Y.S. Choi, Understanding crack formation mechanisms of Ti–48Al–2Cr–2Nb single tracks during laser powder bed fusion, Met. Mater. Int. 27 (2020), https://doi.org/10.1007/s12540-020-00770-1.
[20] P. Gao, W. Huang, H. Yang, G. Jing, Q. Liu, G. Wang, Z. Wang, X. Zeng, Cracking behavior and control of β-solidifying Ti-40Al-9V-0.5Y alloy produced by selective laser melting, J. Mater. Sci. Technol. 39 (2020) 144–154, https://doi.org/10.1016/j.jmst.2019.08.026.
[21] H. Ali, H. Ghadbeigi, K. Mumtaz, Processing parameter effects on residual stress and mechanical properties of selective laser melted Ti6Al4V, J. Mater. Eng. Perform. 27 (2018) 4059–4068, https://doi.org/10.1007/s11665-018-3477-5.
[22] C. Chen, Z. Xiao, Y. Wang, X. Yang, H. Zhu, Prediction study on in-situ reduction of thermal stress using combined laser beams in laser powder bed fusion, Addit. Manuf. 47 (2021), https://doi.org/10.1016/j.addma.2021.102221.
[23] J. Robinson, I. Ashton, P. Fox, E. Jones, C. Sutcliffe, Determination of the effect of scan strategy on residual stress in laser powder bed fusion additive manufacturing, Addit. Manuf. 23 (2018) 13–24, https://doi.org/10.1016/j.addma.2018.07.001.
[24] X. Li, Y. Liu, C. Tan, Y. Zou, Porosity formation mechanisms, microstructure evolution and mechanical performance of AlMgScZr alloy fabricated by laser powder bed fusion: effect of hatch distance, J. Manuf. Process. 94 (2023) 107–119, https://doi.org/10.1016/j.jmapro.2023.03.047.

[25] B. Feng, C. Wang, Q. Zhang, Y. Ren, L. Cui, Q. Yang, S. Hao, Effect of laser hatch spacing on the pore defects, phase transformation and properties of selective laser melting fabricated NiTi shape memory alloys, Mater. Sci. Eng. A 840 (2022), https://doi.org/10.1016/j.msea.2022.142965.
[26] Z. Yao, T. Yang, M. Yang, X. Jia, C. Wang, J. Yu, Z. Li, H. Han, W. Liu, G. Xie, S. Yang, Q. Zhang, C. Wang, S. Wang, X. Liu, Martensite colony engineering: a novel solution to realize the high ductility in full martensitic 3D-printed Ti alloys, Mater. Des. 215 (2022), https://doi.org/10.1016/j.matdes.2022.110445.
[27] M. Wang, Y. Du, H. Wei, W. Liao, From crack-prone to crack-free: eliminating cracks in additively manufactured Ti-48Al-2Cr-2Nb alloy by adjusting phase composition, Mater. Des. 231 (2023), https://doi.org/10.1016/j.matdes.2023.112025.
[28] S.H. Park, O. Gokcekaya, R. Ozasa, M.H. Oh, Y.W. Kim, H.S. Kim, T. Nakano, Microstructure and crystallographic texture evolution of β-solidifying γ-TiAl alloy during single- and multi-track exposure via laser powder bed fusion, Met. Mater. Int. 30 (2024) 1127–1241, https://doi.org/10.1007/s12540-023-01579-4.
[29] B. Duan, Y. Yang, S. He, Q. Feng, L. Mao, X. Zhang, L. Jiao, X. Lu, G. Chen, C. Li, History and development of γ-TiAl alloys and the effect of alloying elements on their phase transformations, J. Alloys Compd. 909 (2022), https://doi.org/10.1016/j.jallcom.2022.164811.
[30] B. Cheng, S. Shrestha, K. Chou, Stress and deformation evaluations of scanning strategy effect in selective laser melting, Addit. Manuf. 12 (2016) 240–251, https://doi.org/10.1016/j.addma.2016.05.007.
[31] T. Todo, T. Ishimoto, O. Gokcekaya, J. Oh, T. Nakano, Single crystalline-like crystallographic texture formation of pure tungsten through laser powder bed fusion, Scr. Mater. 206 (2022) 114252, https://doi.org/10.1016/j.scriptamat.2021.114252.
[32] B. Zhang, Y. Li, Q. Bai, Defect formation mechanisms in selective laser melting: a review, Chin. J. Mech. Eng. 30 (2017) 515–527, https://doi.org/10.1007/s10033-017-0121-5.
[33] H. Gong, K. Rafi, H. Gu, G.D. Janaki Ram, T. Starr, B. Stucker, Influence of defects on mechanical properties of Ti–6Al–4V components produced by selective laser melting and electron beam melting, Mater. Des. 86 (2015) 545–554, https://doi.org/10.1016/j.matdes.2015.07.147.
[34] W. Stopyra, K. Gruber, I. Smolina, T. Kurzynowski, B. Kuźnicka, Laser powder bed fusion of AA7075 alloy: influence of process parameters on porosity and hot cracking, Addit. Manuf. 35 (2020), https://doi.org/10.1016/j.addma.2020.101270.
[35] N. Li, T. Wang, L. Zhang, L. Zhang, Crack initiation mechanism of laser powder bed fusion additive manufactured Al-Zn-Mg-Cu alloy, Mater. Charact. 195 (2023), https://doi.org/10.1016/j.matchar.2022.112415.
[36] M.S. Wang, E.W. Liu, Y.L. Du, T.T. Liu, W.H. Liao, Cracking mechanism and a novel strategy to eliminate cracks in TiAl alloy additively manufactured by selective laser melting, Scr. Mater. 204 (2021) 114151, https://doi.org/10.1016/j.scriptamat.2021.114151.
[37] X. Shi, H. Wang, W. Feng, Y. Zhang, S. Ma, J. Wei, The crack and pore formation mechanism of Ti–47Al–2Cr–2Nb alloy fabricated by selective laser melting, Int. J. Refract. Met. Hard Mater. 91 (2020), https://doi.org/10.1016/j.ijrmhm.2020.105247.
[38] P. Staron, A. Stark, N. Schell, P. Spoerk-Erdely, H. Clemens, Thermal expansion of a multiphase intermetallic Ti-Al-Nb-Mo alloy studied by high-energy X-ray diffraction, Materials 14 (2021) 1–13, https://doi.org/10.3390/ma14040727.
[39] X. Zhang, H. Chen, L. Xu, J. Xu, X. Ren, X. Chen, Cracking mechanism and susceptibility of laser melting deposited Inconel 738 superalloy, Mater. Des. 183 (2019), https://doi.org/10.1016/j.matdes.2019.108105.
[40] S. Waqar, K. Guo, J. Sun, Evolution of residual stress behavior in selective laser melting (SLM) of 316L stainless steel through preheating and in-situ re-scanning techniques, Opt. Laser Technol. 149 (2022), https://doi.org/10.1016/j.optlastec.2021.107806.
[41] X. Luo, C. Yang, Z.Q. Fu, L.H. Liu, H.Z. Lu, H.W. Ma, Z. Wang, D.D. Li, L.C. Zhang, Y.Y. Li, Achieving ultrahigh-strength in beta-type titanium alloy by controlling the melt pool mode in selective laser melting, Mater. Sci. Eng. A 823 (2021), https://doi.org/10.1016/j.msea.2021.141731.
[42] J. Zhou, X. Han, H. Li, S. Liu, J. Yi, Investigation of layer-by-layer laser remelting to improve surface quality, microstructure, and mechanical properties of laser powder bed fused AlSi10Mg alloy, Mater. Des. 210 (2021), https://doi.org/10.1016/j.matdes.2021.110092.
[43] M. Takeyama, S. Kobayashi, Physical metallurgy for wrought gamma titanium aluminides: microstructure control through phase transformations, Intermetallics 13 (2005) 993–999, https://doi.org/10.1016/j.intermet.2004.12.014.
[44] M.V. Pantawane, S. Sharma, A. Sharma, S. Dasari, S. Banerjee, R. Banerjee, N. B. Dahotre, Coarsening of martensite with multiple generations of twins in laser additively manufactured Ti6Al4V, Acta Mater. 213 (2021), https://doi.org/10.1016/j.actamat.2021.116954.
[45] T. Ishimoto, K. Hagihara, K. Hisamoto, S.-H. Sun, T. Nakano, Crystallographic texture control of beta-type Ti–15Mo–5Zr–3Al alloy by selective laser melting for the development of novel implants with a biocompatible low Young's modulus, Scr. Mater. 132 (2017) 34–38, https://doi.org/10.1016/j.scriptamat.2016.12.038.
[46] X. Luo, T. Song, A. Gebert, K. Neufeld, I. Kaban, H. Ma, W. Cai, H. Lu, D. Li, N. Li, Y. Li, C. Yang, Programming crystallographic orientation in additive-manufactured beta-type titanium alloy, Adv. Sci. 10 (2023), https://doi.org/10.1002/advs.202302884.
[47] W.G. Burgers, On the process of transition of the cubic-body-centered modification into the hexagonal-close-packed modification of zirconium, Physica 1 (1934) 561–586, https://doi.org/10.1016/S0031-8914(34)80244-3.
[48] T.B. Massalski, Massive transformations revisited, Metall. Mater. Trans. A 33 (2002) 2277–2283.
[49] S.H. Park, R. Ozasa, O. Gokcekaya, K. Cho, H.Y. Yasuda, M.-H. Oh, Y.-W. Kim, T. Nakano, Effect of cooling rate on powder characteristics and microstructural evolution of gas atomized β-solidifying γ-TiAl alloy powder, Mater. Trans. 65 (2024) 199–204, https://doi.org/10.2320/matertrans.mt-m2023174.
[50] S.H. Park, O. Gokcekaya, R. Ozasa, K. Cho, H.Y. Yasuda, M.H. Oh, T. Nakano, Microstructure evolution of gas-atomized β-solidifying γ-TiAl alloy powder during subsequent heat treatment, Crystals 13 (2023), https://doi.org/10.3390/cryst13121629.
[51] D. Hu, H. Jiang, Martensite in a TiAl alloy quenched from beta phase field, Intermetallics 56 (2015) 87–95, https://doi.org/10.1016/j.intermet.2014.09.007.
[52] M. Schloffer, F. Iqbal, H. Gabrisch, E. Schwaighofer, F.P. Schimansky, S. Mayer, A. Stark, T. Lippmann, M. Göken, F. Pyczak, H. Clemens, Microstructure development and hardness of a powder metallurgical multi phase γ-TiAl based alloy, Intermetallics 22 (2012) 231–240, https://doi.org/10.1016/j.intermet.2011.11.015.
[53] N. Hansen, Hall-petch relation and boundary strengthening, Scr. Mater. 51 (2004) 801–806, https://doi.org/10.1016/j.scriptamat.2004.06.002.
[54] H. Inui, Y. Toda, M. Yamaguchi, Plastic deformation of single crystals of a DO19 compound with an off-stoichiometric composition (Ti-36·5 at.% Al) at room temperature, Philos. Mag. A 67 (1993) 1315–1332, https://doi.org/10.1080/01418619308225357.
[55] B. Zhu, X. Xue, H. Kou, X. Li, J. Li, Effect of microstructure on the fracture toughness of multi-phase high Nb-containing TiAl alloys, Intermetallics 100 (2018) 142–150, https://doi.org/10.1016/j.intermet.2018.06.014.
[56] W. Li, J. Liu, Y. Zhou, S. Wen, J. Tan, S. Li, Q. Wei, C. Yan, Y. Shi, Texture evolution, phase transformation mechanism and nanohardness of selective laser melted Ti-45Al-2Cr-5Nb alloy during multi-step heat treatment process, Intermetallics 85 (2017) 130–138, https://doi.org/10.1016/j.intermet.2017.01.016.
[57] Y. Umakoshi, T. Nakano, T. Yamane, The effect of orientation and lamellar structure on the plastic behavior of TiAl crystals, Mater. Sci. Eng. A 152 (1992) 81–88, https://doi.org/10.1016/0921-5093(92)90050-B.
[58] Y. Umakoshi, T. Nakano, T. Takenaka, K. Sumimoto, T. Yamane, Orientation and temperature dependence of yield stress and slip geometry of $Ti_3Al$ and $Ti_3Al$-V single crystals, Acta Metall. Mater. 41 (1993) 1149–1154.